sciendo
Power Electronics and Drives
Volume 9(44), 2024 DOI: 10.2478/pead-2024-0033

Simulating Rolling Element Bearing Defects in Induction Machines

Research paper

Florian Floh[1,*], Helmut Weiss[1], Markus Makoschitz[2]

[1]*Chair of Electrical Engineering, Montanuniversitaet Leoben, Austria*
[2]*Chair of Electrical Engineering, Montanuniversitaet Leoben, Austria and Austrian Institute of Technology, Vienna*

Received: 28 May 2024; Accepted: 30 September 2024

Abstract: The significant occurrence of bearing faults in electrical machines necessitates continuous online monitoring of the machine's operating data with the main objective of ensuring both high reliability and efficiency and therefore minimising the chance of unwanted breakdowns. This work focuses on the simulation of (defective) bearings, utilising a dedicated model with five degrees of freedom (DOF) (translational motion) in conjunction with an induction motor model. The primary objective is to gain a comprehensive understanding of how faulty bearings influence both the entire bearing itself and the machine, mainly concerning vibration signals and additional frictional torque. Additionally, various shapes of spalls on the raceway(s) are described, analysed and compared. This work is an extended version of the conference paper 'Simulating Rolling Element Bearing Defects in Induction Machines', presenting additional information on how to simulate spalls (with different shapes and sizes) on the inner ring of the bearing. Furthermore, the so-obtained vibration signal is examined and a method is proposed aiming to verify the simulation results and to predict the location of the spall (raceway of the inner or outer ring).

Keywords: *condition monitoring • bearing faults • bearing fault detection • induction machine*

1. Introduction

Since its invention in the late 19th century, persistent endeavours have been taken for the development of the induction motor, while the primary focus includes increasing both its reliability and the overall efficiency. Contemporary industrial applications are designed that the induction motor is fed by an inverter, facilitating variable speeds of the output shaft and greater torque during start-ups (Fischer, 1995; Giersch et al., 1991).

Although inverter-fed induction machines serve as a robust drive system solution, common breakdowns often originate from stator and/or rotor winding failures, defective bearings, irregularities in the air gap or faulty auxiliary parts (such as fan blades) (Strangas et al., 2022). As illustrated in Figure 1, bearing faults emerge as the foremost cause for breakdowns, accounting for approximately 40% of breakdowns in high power motors (especially in petrochemical applications). In low- and medium-power electric motors, bearing faults are responsible for 8% of breakdowns, as can be seen in Figure 2.

Among various factors, bearing defects are primarily due to the result of contamination of the mating surfaces with foreign solid particles, inadequate or absent lubrication, corrosion, excessive loads or misalignment (during the installation). To elevate the efficiency and operational reliability of electrical machines (especially induction motors), detection of occurring faults at an early stage is a key factor for decreasing the chance of a potential breakdown of the entire drive system (Nandi et al., 2005; Strangas et al., 2022).

Figure 3 provides a thorough insight into how various fault types affect the frictional torque created by the examined bearing and compares it to the 'healthy' one. During the testing procedure, the quantities that are

* *Email: florian.floh@unileoben.ac.at*

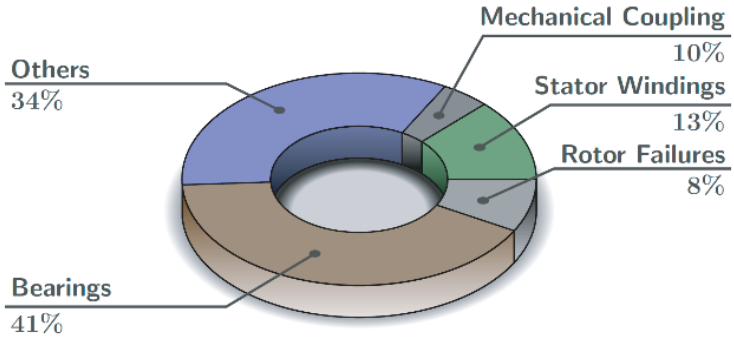

Figure 1. Prevalence of different fault types in high power motors in petrochemistry, derived from Floh and Weiss (2023) and Thorsen and Dalva (1995).

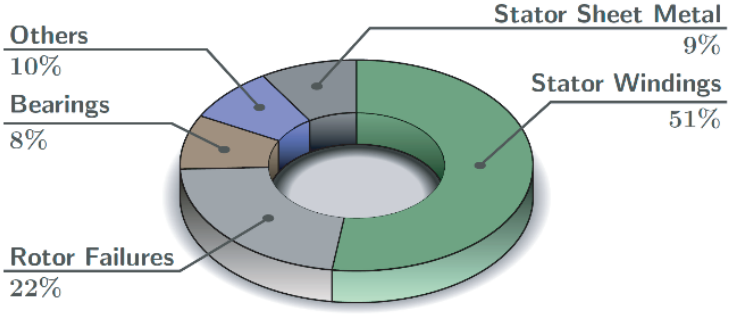

Figure 2. Prevalence of different fault types in low and medium power motors, derived from Floh and Weiss (2023) and Strangas et al. (2022).

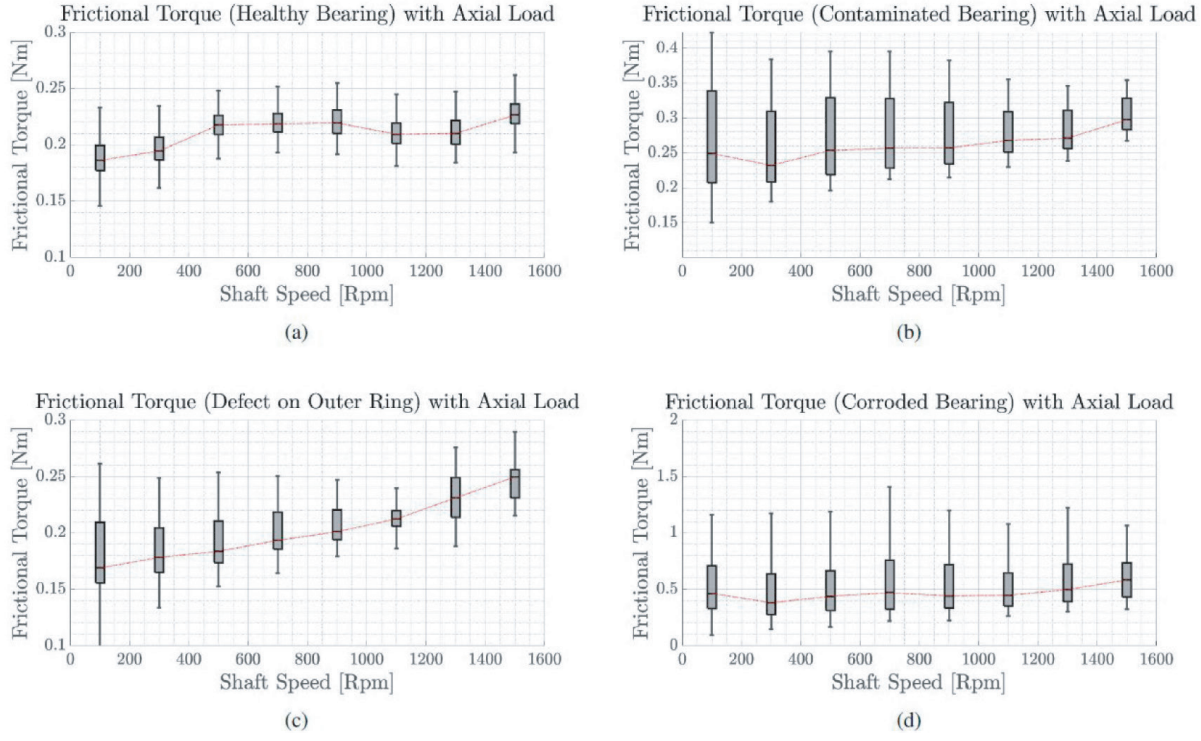

Figure 3. Comparison of the frictional torques of a healthy bearing (a), with defective ones (b–d). Measured with a real 0.37 kW machine. Adapted from Floh and Weiss (2023).

measured and tracked are the torque (using a torque transducer) and the shaft speed, while the investigated bearings are subjected to an axial load. In this illustration, the substantial difference in frictional torque between the corroded bearing (Figure 3d) and the healthy one (Figure 3a) is attributed to the entire absence of lubrication and the extensive level of corrosion present in both the inner and the outer raceway, as well as the cage and the rolling elements. Results of the examined contaminated bearing are depicted in Figure 3b. This bearing is subjected to a contamination of solid metal particles of size less than 1 mm. Data gathered from the bearing that exhibits a defect on the outer ring, to be more specific, a spall that measures approximately 1.4 mm in width (perpendicular to the raceway) and 1 mm in depth, are shown in Figure 3c.

One important aspect, which has to be emphasised, is shown in Figure 3, in which the upper and lower lines of the boxes characterise the upper and lower quartiles denoting 0.75 and 0.25 quantiles, respectively. The horizontal lines within the boxes represent the median values, which are connected to each other via a red line. In addition to this, the non-outlier maximum and minimum values are indicated by the vertical lines extending above and below the upper and lower quartiles (Floh and Weiss, 2023).

To obtain a deeper understanding of how various bearing faults impact induction machines, such as increased frictional torques and vibration, the authors propose a further extension of a dynamic bearing model, where the localised faults on the inner and/or outer raceway are simulated in different shapes (triangular and parabolic), yielding more realistic results regarding the vibrational signal.

In addition to this, the so-obtained numerical data are then compared to similar faults in a real bearing application, which illustrates that both findings do agree well in the case of parabolic-shaped faults (both on the inner and outer raceway of the examined bearing).

However, defective bearings do not necessarily have to result in a breakdown of the entire machine. In an early stage of an occurring fault, the efficiency of the examined motor is decreased, as a consequence of the additional frictional torque, as depicted in Figure 4. The investigated bearings were deep groove ball bearing (6203-Z), mounted in an induction machine with a rated output power of 0.37 kW. A variable torque load was applied with the help of an eddy current brake and measured with a torque transducer.

For instance, comparison of a machine with a healthy bearing to that with a contaminated (with solid particles of size <1 mm) bearing illustrates that the efficiency in the nominal operating point (approximately 1415 rpm and 2.5 Nm) decreases from 71% to approximately 67.5% for the faulty one (see Figure 4). The same phenomenon can also be found with other defects, as depicted in Figures 3c,d.

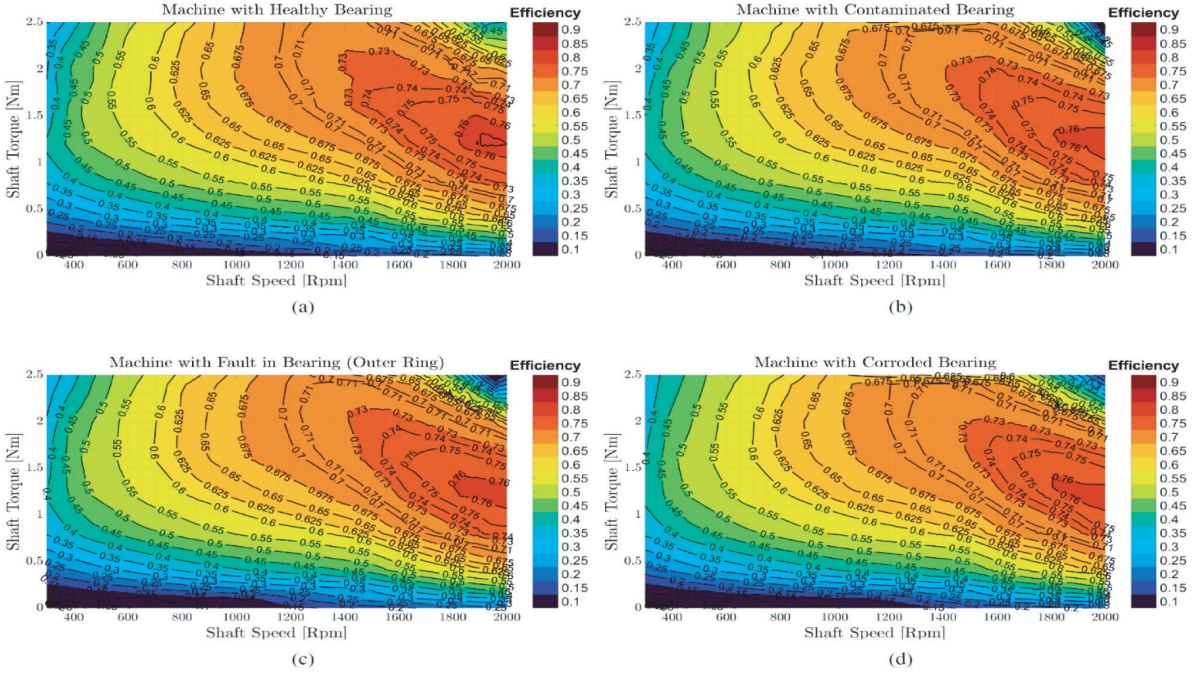

Figure 4. Comparison of the efficiency of a machine with healthy bearings (a) to that with defective ones (b–d). Measurements taken in a real 0.37 kW induction machine.

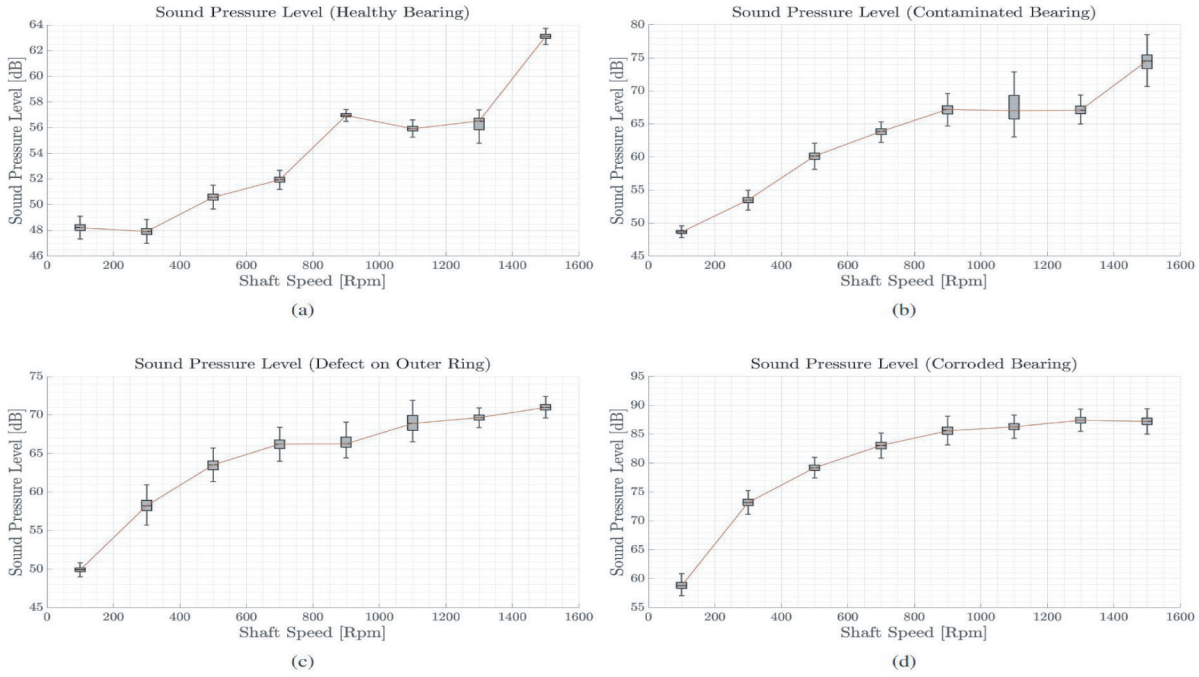

Figure 5. Comparison of the SPL of a machine with healthy bearings (a) to that with defective ones (b–d), measured at a distance of 1 m from the examined machine. SPL, sound pressure level.

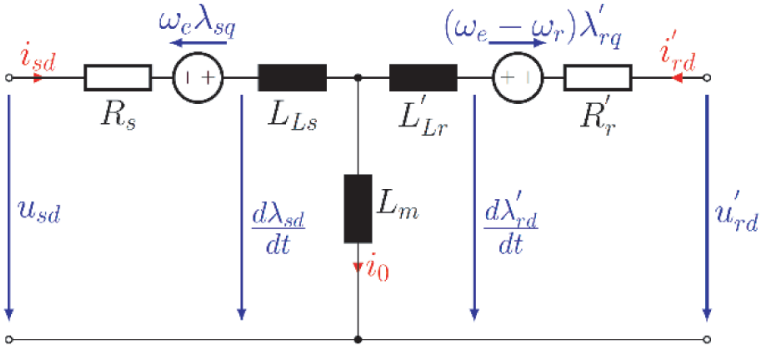

Figure 6. T-type dq-equivalent circuit (d-axis) of an induction machine. Adapted from Gonzalo (2017).

Furthermore, another issue that arises in a machine with defective bearings is an increase in sound pressure level (SPL), which is shown in Figure 5. The relatively high SPL of the corroded bearing compared to the healthy one is explained by the complete lack of lubricant and corroded mating surfaces inside the bearing.

2. Dynamic Model of an Induction Machine

The first step of this proposed method consists of modelling the induction motor (with previously identified parameters from a 0.37 kW machine) in the MATLAB/Simulink R2022b from MathWorks environment. The required (differential) equations for the model are derived from the T-type equivalent circuits (as illustrated in Figures 6 and 7), both in direct axis (d-axis) and quadrature axis (q-axis). The superscripts on the rotor side of the equivalent circuits (right-hand side) indicate that these quantities are referenced to the stator side. In addition to this, the subscripts *r*, *s, d* and *q* denote that these quantities refer to the rotor, stator and d- and q-axes, respectively (Floh and Weiss, 2023).

Here, the resistances and inductances of both rotor and stator are assumed to be constant and state-independent, which still yields comparable results with the real machine, as used in the scope of this work. However, if one wants

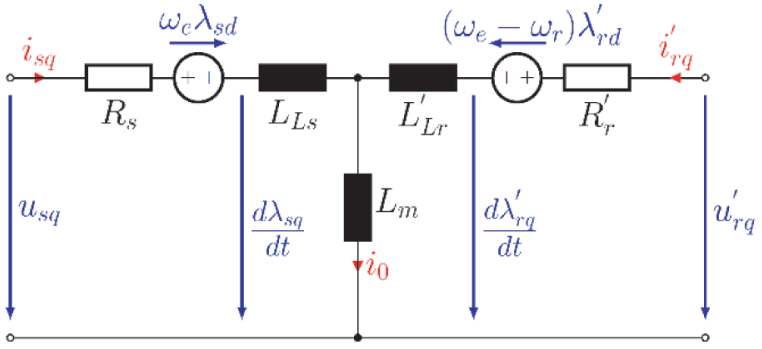

Figure 7. T-type dq-equivalent circuit (q-axis) of an induction machine. Adapted from Gonzalo (2017).

to consider non-linearities, such as iron losses, magnetic saturation or current displacement, Quang and Dittrich (2008) provided an overview on how to include them in the model.

By applying Kirchhoff's law to the left side of the T-type equivalent circuits (both on d- and q-axes), the following equations can be derived:

$$-u_{sd} + i_{sd}R_s - \omega_e \lambda_{sq} + \frac{d\lambda_{sd}}{dt} = 0 \tag{1}$$

$$-u_{sq} + i_{sq}R_s - \omega_e \lambda_{sd} + \frac{d\lambda_{sq}}{dt} = 0 \tag{2}$$

The same procedure can be performed on the right-hand side (rotor side):

$$-u'_{rd} + i'_{rd}R'_r - (\omega_e - \omega_r)\lambda'_{rq} + \frac{d\lambda'_{rd}}{dt} = 0 \tag{3}$$

$$-u'_{rq} + i'_{rq}R'_r - (\omega_e - \omega_r)\lambda'_{rd} + \frac{d\lambda'_{rq}}{dt} = 0 \tag{4}$$

Voltages applied to the stator are characterised by u_{sd} and u_{sq}, whereby the rotor voltages (referenced to the stator side) are represented by u'_{rd} and u'_{rq}. Considering an induction motor with a squirrel cage rotor, u'_{rd} and u'_{rq} are equal to zero, since the rotor bars are shortened on both ends, which results in a negligible voltage drop. The resistances of the stator and rotor windings are represented by R_s and R'_r. The quantities i_{sd}, i_{sq}, i'_{rd} and i'_{rq} characterise the currents, whereas λ_{sd}, λ_{sq}, λ'_{rd} and λ'_{rq} characterise the flux linkages of the stator and rotor, respectively. In addition to this, ω_r and ω_e represent the rotational speed of the rotor and that of the reference frame (Leedy, 2013).

To obtain a more compact representation of Eqs (1)–(4), they can be written in matrix-form as follows:

$$\frac{d}{dt}\begin{bmatrix}\lambda_{sd}\\ \lambda_{sq}\end{bmatrix} = \begin{bmatrix}u_{sd}\\ u_{sq}\end{bmatrix} - R_s\begin{bmatrix}i_{sd}\\ i_{sq}\end{bmatrix} + \omega_e\begin{bmatrix}0 & 1\\ -1 & 0\end{bmatrix}\begin{bmatrix}\lambda_{sd}\\ \lambda_{sq}\end{bmatrix} \tag{5}$$

$$\frac{d}{dt}\begin{bmatrix}\lambda'_{rd}\\ \lambda'_{rq}\end{bmatrix} = \begin{bmatrix}u'_{rd}\\ u'_{rq}\end{bmatrix} - R'_r\begin{bmatrix}i'_{rd}\\ i'_{rq}\end{bmatrix} + (\omega_e - \omega_r)\begin{bmatrix}0 & 1\\ -1 & 0\end{bmatrix}\begin{bmatrix}\lambda'_{rd}\\ \lambda'_{rq}\end{bmatrix} \tag{6}$$

To describe the flux linkages of the rotor and stator, their self-inductances L_r and L_s need to be formulated with the help of their leakage inductances L_{L_s} and L_{L_R} as well as their mutual inductance L_m (Leedy, 2013):

$$L_s = L_{L_s} + L_m \tag{7}$$

$$L_r = L_{L_r} + L_m \tag{8}$$

Therefore, the equations of the flux linkages can be described in the following manner (Leedy, 2013):

$$\lambda_{sd} = i_{sd} L_s + i'_{rd} L_m \tag{9}$$

$$\lambda_{sq} = i_{sq} L_s + i'_{rq} L_m \tag{10}$$

$$\lambda'_{rd} = i'_{rd} L_r + i_{sd} L_m \tag{11}$$

$$\lambda'_{rq} = i'_{rq} L_r + i_{sq} L_m \tag{12}$$

Again, Eqs (9)–(12) can be represented in a more compact manner, which yields:

$$\begin{bmatrix} \lambda_{sd} \\ \lambda_{sq} \\ \lambda'_{rd} \\ \lambda'_{rq} \end{bmatrix} = \begin{bmatrix} L_s & 0 & L_m & 0 \\ 0 & L_s & 0 & L_m \\ L_m & 0 & L_r & 0 \\ 0 & L_m & 0 & L_r \end{bmatrix} \begin{bmatrix} i_{sd} \\ i_{sq} \\ i'_{rd} \\ i'_{rq} \end{bmatrix} \tag{13}$$

Next, the currents i_{sd}, i_{sq}, i'_{rd} and i'_{rq} can be represented by rearranging Eqs (9)–(12):

$$i_{sd} = \frac{\lambda_{sd} - i'_{rd} L_m}{L_s} \tag{14}$$

$$i_{sq} = \frac{\lambda_{sq} - i'_{rq} L_m}{L_s} \tag{15}$$

$$i'_{rd} = \frac{\lambda'_{rd} - i_{sd} L_m}{L_r} \tag{16}$$

$$i'_{rq} = \frac{\lambda'_{rq} - i_{sq} L_m}{L_r} \tag{17}$$

To get the currents in an explicit manner, Eqs (14)–(17) have to be inserted into each other, which yields:

$$i_{sd} = \frac{L_r}{L_s L_r - L_m^2} \lambda_{sd} - \frac{L_m}{L_s L_r - L_m^2} \lambda'_{rd} \tag{18}$$

$$i_{sq} = \frac{L_r}{L_s L_r - L_m^2} \lambda_{sq} - \frac{L_m}{L_s L_r - L_m^2} \lambda'_{rq} \tag{19}$$

$$i'_{rd} = \frac{L_s}{L_s L_r - L_m^2} \lambda'_{rd} - \frac{L_m}{L_s L_r - L_m^2} \lambda_{sd} \tag{20}$$

$$i'_{rq} = \frac{L_s}{L_s L_r - L_m^2} \lambda'_{rq} - \frac{L_m}{L_s L_r - L_m^2} \lambda_{sq} \tag{21}$$

Rearranging Eqs (18)–(21) in matrix form yields a more compact representation:

$$\begin{bmatrix} i_{sd} \\ i_{sq} \\ i'_{rd} \\ i'_{rq} \end{bmatrix} = \frac{1}{L_s L_r - L_m^2} \begin{bmatrix} L_r & 0 & -L_m & 0 \\ 0 & L_r & 0 & -L_m \\ -L_m & 0 & L_s & 0 \\ 0 & -L_m & 0 & L_s \end{bmatrix} \begin{bmatrix} \lambda_{sd} \\ \lambda_{sq} \\ \lambda'_{rd} \\ \lambda'_{rq} \end{bmatrix} \tag{22}$$

Finally, to obtain the desired differential equations that are the bases of the Simulink model, Eqs (1)–(4) have to be rearranged and inserted into Eqs (18)–(21), resulting in:

$$\frac{d\lambda_{sd}}{dt} = u_{sd} - \left(\frac{L_r \lambda_{sd} - L_m \lambda'_{rd}}{L_s L_r - L_m^{\,2}} \right) R_s + \omega_e \lambda_{sq} \tag{23}$$

$$\frac{d\lambda_{sq}}{dt} = u_{sq} - \left(\frac{L_r \lambda_{sq} - L_m \lambda'_{rq}}{L_s L_r - L_m^{\,2}} \right) R_s - \omega_e \lambda_{sd} \tag{24}$$

$$\frac{d\lambda'_{rd}}{dt} = u'_{rd} - \left(\frac{L_s \lambda'_{rd} - L_m \lambda_{sd}}{L_s L_r - L_m^{\,2}} \right) R'_r + \left(\omega_e - \omega_r \right) \lambda'_{rq} \tag{25}$$

$$\frac{d\lambda'_{rq}}{dt} = u'_{rq} - \left(\frac{L_s \lambda'_{rq} - L_m \lambda_{sq}}{L_s L_r - L_m^{\,2}} \right) R'_r + \left(\omega_e - \omega_r \right) \lambda'_{rd} \tag{26}$$

In the case of a squirrel-cage rotor, the voltages u'_{rd} and u'_{rq} vanish due to the rotor bars shortened at both ends (Leedy, 2013).

After obtaining the currents i_{sd}, i_{sq}, i'_{rd} and i'_{rq}, the electromagnetic torque T_{em} is computed in the following manner:

$$T_{em} = \frac{3}{2} p L_m \left(i_{sq} i'_{rd} - i_{sd} i'_{rq} \right), \tag{27}$$

where the quantity p represents the number of pole pairs of the examined machine (Leedy, 2013).

The net output torque on the shaft is computed by taking the load torque T_L, the frictional torque T_{Fric} and the rotor inertia J into consideration (Krishnan, 2001):

$$T_{net} = T_{em} - \left(T_L + J \frac{d\omega_r}{dt} + T_{Fric} \right) \tag{28}$$

Any additional frictional torque T_{Fric}, which is attributable to a defective bearing inside the machine, can therefore be considered in Eq. (28).

The previously described equations included quantities (currents and voltages), which are referenced to the dq reference frame. To convert the voltage sources from the abc system to the $\alpha\beta$ frame in the first step, the so-called 'Direct Clark Transform' can be applied (Gonzalo, 2017):

$$\begin{bmatrix} u_\alpha \\ u_\beta \\ u_0 \end{bmatrix} = \frac{2}{3} \begin{bmatrix} 1 & -\frac{1}{2} & -\frac{1}{2} \\ 0 & \frac{\sqrt{3}}{2} & -\frac{\sqrt{3}}{2} \\ \frac{1}{2} & \frac{1}{2} & \frac{1}{2} \end{bmatrix} \begin{bmatrix} u_a \\ u_b \\ u_c \end{bmatrix} \tag{29}$$

Converting the quantities u_α and u_β from the stationary frame to the synchronous reference frame is achieved via the following transformation (Gonzalo, 2017):

$$\begin{bmatrix} u_d \\ u_q \end{bmatrix} = \begin{bmatrix} \cos(\theta) & -\sin(\theta) \\ \sin(\theta) & \cos(\theta) \end{bmatrix} \begin{bmatrix} u_\alpha \\ u_\beta \end{bmatrix} \tag{30}$$

3. Modelling of a Rolling Element Bearing

According to Sawalhi and Randall (2008), describing the dynamic behaviour of a rolling element bearing in a model dates back to the work of Lundberg and Palmgren (1947). The core statement of their publication covers the

modelling of both radial and axial deflections in the presence of a corresponding load with the help of non-linear stiffness coefficients. However, one downside of this approach is the lack of characterising the non-linear nature of the bearing.

As stated by Howard (1994), an improvement in the field of dynamic modelling of a rolling element bearing (specifically in angular contact ball bearings) has been achieved by the work of Gupta (1975). In the scope of this publication, the author formulates and solves the generalised differential equations of motion for the rolling element(s) with given initial conditions. Therefore, the motion of the rolling element (ball type) both in transient and steady state was described, which furthermore allowed the prediction of the amount of skid between the mating surfaces and therefore the rate of wear. An extension of this work, which covers cylindrical roller bearings, can be found in a study by Gupta (1979).

A detailed implementation and discussion of localised and distributed defects (such as waviness on the raceway's surface) is shown in the work of Sopanen and Mikkola (2003a,b). The gist of their publication is, among others, that a low-order waviness of the raceway's profile (also termed 'out-of-roundness') yields vibrations with frequencies at orders of the occurring waviness times the rotational shaft speed, while a waviness in the order of the number of rolling elements results in vibration at the bearing defect frequencies.

The characteristic defect frequencies (ball pass frequency of the inner/outer ring) are further explained in Section 4.

A more detailed summary of (current) literature on dynamic modelling of rolling element bearings is provided by Kumbhar et al. (2021).

The proposed model of a rolling element bearing here is based on the work of Mishra et al. (2017) and Sawalhi and Randall (2008), having five degrees of freedom (DOF) in translational motion and one degree of freedom in rotational motion. However, the latter one is of minor relevance in the scope of this work.

As illustrated in Figure 8, the bearing's outer ring is seated in an housing with given stiffness k_H and damping coefficient b_H, which is capable of moving in the x- and y-directions. Separating the outer ring from the inner one and allowing the latter one to perform a rotation with low friction is achieved by the rolling elements with a given stiffness k_{RE}. In addition, the inner ring is attached to the shaft with a tight fit. Consequently, there is no relative rotation possible between these mentioned parts (Mishra et al., 2017; Sawalhi and Randall, 2008).

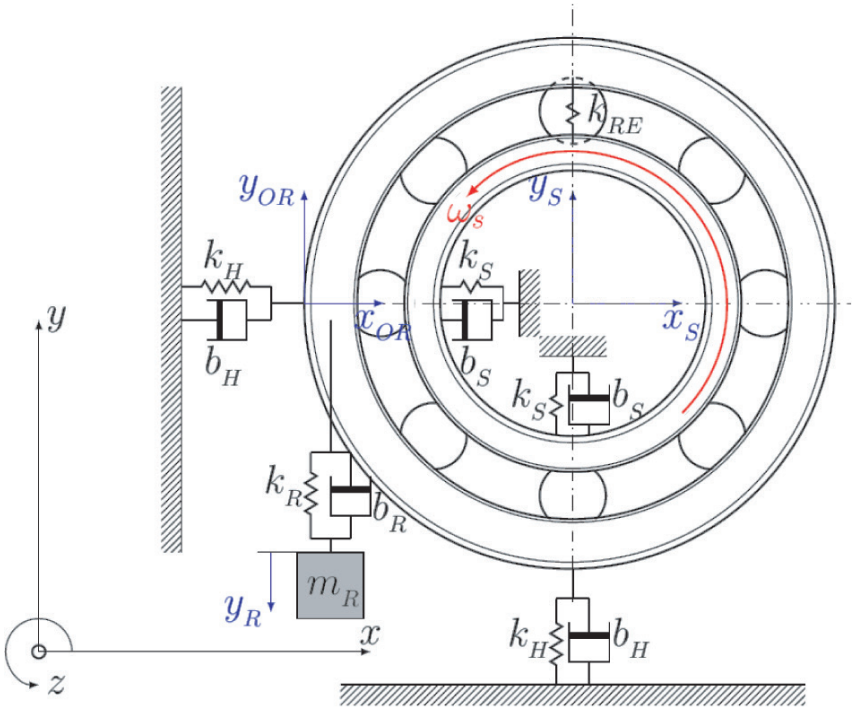

Figure 8. Schematic overview of the five DOF (translational motion) bearing model. Adapted from Mishra et al. (2017) and Sawalhi and Randall (2008). DOF, degrees of freedom.

To derive the equations of motion for the five DOF bearing model, the following assumptions (see [Mishra et al., 2017; Sawalhi and Randall, 2008]) have to be taken into consideration:

- The housing, which accommodates the bearing, is kept in a fixed position, meaning it has no DOF (neither rotational nor translational motion).
- The outer ring has two DOF (translational motion) along its x- and y-axes. Therefore, no rotation around any axis is allowed.
- Both the shaft and the inner ring are capable of performing a motion in the x- and y-axes and a rotation around the z-axis. Any rotations around the other remaining axes are not possible.
- The main objective of the cage is to keep the rolling elements separated from each other, with a constant angle between each other.
- Any surfaces that are in contact with each other (inner raceway/rolling elements, outer raceway/rolling elements) have to obey the Hertzian contact model.

In the first step, the rotational speed of the cage ω_c can be derived with the help of the angular speed of the machine's rotor (Smagala and Kecik, 2019):

$$\omega_c = \dot{\varphi}_c = \frac{\omega_s}{2}\left(1 - \frac{D_{RE}}{D_{\text{Pitch}}}\right) \tag{31}$$

In this equation, the quantities D_{Pitch} and D_{RE} represent the pitch diameter (the diameter between the centres of the rolling elements) and the diameter of the rolling element (in this case, ball-shaped ones), respectively.

Additionally, to obtain the angular position of the cage, the following relationship has to be taken into consideration:

$$\varphi_c = \frac{\varphi_s}{2}\left(1 - \frac{D_{RE}}{D_{\text{Pitch}}}\right) \tag{32}$$

Here, the constant φ_s denotes the angular position of the inner ring (and therefore the shaft).

To obtain each individual angle of the rolling elements (the *i*-th element), the following equation can be derived from the previous ones (Sawalhi and Randall, 2008):

$$\varphi_i = \frac{2\pi(i-1)}{n_{RE}} + \omega_c t + \varphi_{c0} + \underbrace{(0.5 - \text{rand})\varphi_{\text{slip}}}_{\text{Slippage}} \tag{33}$$

The quantities φ_{c0} and n_{RE} denote the initial position of the cage and the number of rolling elements in the bearing, respectively. To account for the angular deviation, which occurs due to slippage between the mating surfaces inside the bearing, the slippage can be modelled as described by Sawalhi and Randall (2008). Typical values for φ_{slip} are in the range of 0.001–0.002 rad.

Finally, the rotational speed of the individual rolling elements, which can be beneficial for the examination of faults in the outer ring, is given by:

$$\dot{\varphi}_{RE,\text{spin}} = \omega_{RE,\text{spin}} = \frac{\omega_s}{2}\frac{D_{\text{Pitch}}}{D_{RE}}\left(1 - \left(\frac{D_{RE}}{D_{\text{Pitch}}}\cos(\alpha)\right)^2\right) \tag{34}$$

In this context, the constant α denotes the contact angle between the rolling element and the raceway (Sawalhi and Randall, 2008).

3.1. Equations of motion of the five DOF model

Based on the image of the bearing in Figure 8 and the assumptions mentioned at the beginning of Section 3, the following five equations of motion can be formulated (Mishra et al., 2017; Sawalhi and Randall, 2008).

Equation of motion of the outer ring (in the x-direction):

$$m_H \ddot{x}_{OR} + b_H \dot{x}_{OR} + k_H x_{OR} = F_x \tag{35}$$

Equation of motion of the outer ring (in the y-direction):

$$m_H \ddot{y}_{OR} + \left(b_H + b_R\right)\dot{y}_{OR} + \left(k_H + k_R\right)y_{OR} - k_R y_R - b_R \dot{y}_R = F_y - m_H g \tag{36}$$

Equation of motion of the shaft (in the x-direction):

$$m_s \ddot{x}_s + b_s \dot{x}_s + k_s x_s = -F_x \tag{37}$$

Equation of motion of the shaft (in the y-direction):

$$m_s \ddot{y}_s + b_s \dot{y}_s + k_s x_s = -F_y - m_s g \tag{38}$$

Equation of motion of the mass attached to the outer ring (in the y-direction):

$$m_R \ddot{y}_R + b_R\left(-\dot{y}_{OR} + \dot{y}_R\right) + k_R\left(-y_{OR} + y_R\right) = -m_R g \tag{39}$$

In Eqs (35)–(39), the quantities m_H, m_R and m_s denote the mass of the bearing's housing, the attached mass and the shaft (including the inner ring), respectively. Additionally, b_H, b_R and b_s represent the damping coefficient, and k_H, k_R and k_S represent the stiffness of the housing, the attached mass and the shaft.

Here, the main objective of attaching a mass to the outer ring is the possibility of simulating the typical response of the examined bearing (Sawalhi and Randall, 2008).

3.2. Modelling of the contact forces

The contact forces occurring between the mating forces inside the bearing can be modelled by means of the Hertzian contact model, both in the horizontal and vertical directions:

$$F_x = k_{RE}\sum_{i=1}^{n_{RE}} \delta_i^{\gamma} \cos\left(\varphi_i\right) H\left(-\delta_i\right) \tag{40}$$

$$F_y = k_{RE}\sum_{i=1}^{n_{RE}} \delta_i^{\gamma} \sin\left(\varphi_i\right) H\left(-\delta_i\right) \tag{41}$$

In this context, the constant k_{RE} characterises the spring stiffness of the rolling elements. Furthermore, δ_i denotes the contact deformation on the mating surfaces caused by the *i*-th rolling element. When examining bearings with a cylindrical-shaped rolling element, the exponent γ is equal to $\frac{10}{9}$ and $\frac{3}{2}$ for those with ball-shaped ones (Smagala and Kecik, 2019).

The computation of the contact deformation in a bearing without a defect is achieved as suggested by Smagala and Kecik (2019):

$$\delta_i = \left(x_s - x_{OR}\right)\cos\left(\varphi_i\right) + \left(y_s - y_{OR}\right)\sin\left(\varphi_i\right) - c, \tag{42}$$

where the clearance inside the bearing is represented by the constant c. The relative translational motion performed between the shaft and the outer ring in x- and y-directions is represented by the terms $\left(x_s - x_{OR}\right)$ and $\left(y_s - y_{OR}\right)$, respectively.

An important aspect, which has to be taken into consideration, is that the contact forces F_x and F_y can only appear in the load zone of the examined bearing (see Figure 9). Consequently, deformations of the mating surfaces can only occur in the load zone, i.e. the part of the bearing that is subjected to compressive forces. This fact is considered by including the Heaviside function in Eqs (40) and (41) (Mishra et al., 2017):

$$H\left(x\right) = \begin{cases} 0 \; x < 0 \\ 1 \; x \geq 0 \end{cases} \tag{43}$$

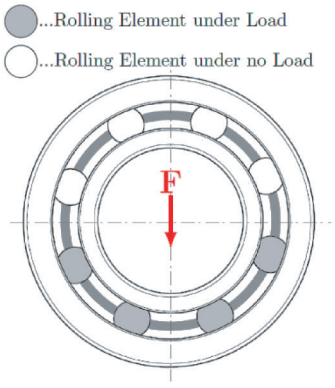

Figure 9. Visualisation of the bearing's load zone. Adapted from Mishra et al. (2017).

Modelling a defective bearing can be achieved, if Eq. (42) is modified in the following manner:

$$\delta_i = (x_s - x_{OR})\cos(\varphi_i) + (y_s - y_{OR})\sin(\varphi_i) - c - h(\varphi_i), \tag{44}$$

where $h(\varphi_i)$ characterises the height of the spall (this will be discussed more thoroughly in the following subsection).

The additional frictional torque T_{Fric} that is caused by a defect in the bearing (for instance, on the inner/outer ring or the rolling element) can be derived from the contact forces F_{Ni} that are perpendicular to the raceway(s). These contact forces themselves can be computed from F_x and F_y. Therefore, this frictional torque is obtained as follows (Meinel, 2020):

$$T_{\text{Fric}} = \mu\, r \sum_{i=1}^{n_{RE}} F_{Ni} \tag{45}$$

3.3. Modelling of a fault on the outer ring of a bearing

So far, defective bearings were widely modelled with a simple rectangular spall on either of the raceways, as suggested by different publications in this research area. Hence, the rolling element rather 'falls' into the spall, rather than gradually entering it, as it would be the case in a 'real' defective bearing.

Another important aspect that has to be considered is the fact that defects in a bearing are usually small compared to that in the rolling element. Therefore, only a fraction of the said rolling element is capable of entering the spall, when passing. The procedure of determining the depth $h(\varphi)$ of the rolling element entering is discussed below.

In the case of a triangular-shaped spall, as depicted in Figure 10, and a void with length s, $h(\varphi)$ is given as follows:

If $\varphi_{def} \leq \varphi \leq \left(\varphi_{def} + \frac{\Delta\varphi}{2}\right)$:

$$h(\varphi) = \left[\frac{D_{RE}}{2} - \sqrt{\frac{D_{RE}^2}{4} - \frac{s^2}{4}}\right]\frac{2}{\Delta\varphi}\left(\varphi - \varphi_{def}\right) \tag{46}$$

If $\left(\varphi_{def} + \frac{\Delta\varphi}{2}\right) \leq \varphi \leq \left(\varphi_{def} + \Delta\varphi\right)$:

$$h(\varphi) = \left[\frac{D_{RE}}{2} - \sqrt{\frac{D_{RE}^2}{4} - \frac{s^2}{4}}\right]\frac{2}{\Delta\varphi}\left(\varphi_{def} + \Delta\varphi - \varphi\right) \tag{47}$$

In Eqs. (46) and (47), the quantities φ, φ_{def} and $\Delta\varphi$ denote the current angle of the examined rolling element, the angle of the occurring defect and the angular dimension of the occurring defect, respectively.

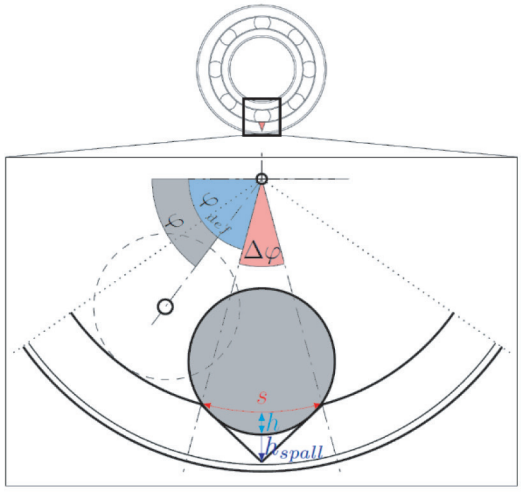

Figure 10. Illustration on how a rolling element approaches and enters a triangular spall in the outer ring. The dimensions of the spall are exaggerated for better demonstration. Adapted from Floh and Weiss (2023).

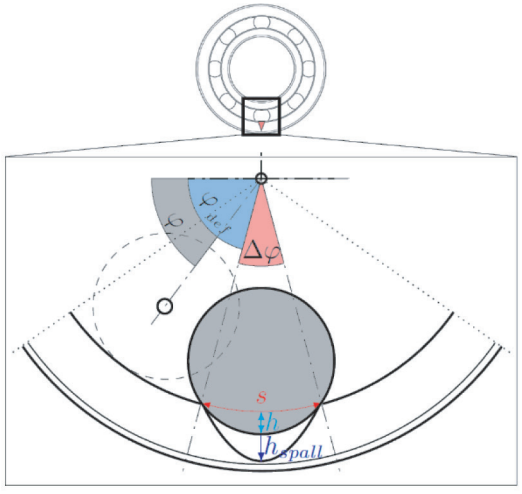

Figure 11. Illustration on how a rolling element approaches and enters a parabolic spall in the outer ring. The dimensions of the spall are exaggerated for better demonstration. Adapted from Floh and Weiss (2023).

However, if defects like electrical pitting are considered, where the pits or grooves rather resemble a spall with a parabolic shape (as depicted in Figure 11), the following procedure for the computation of $h(\varphi)$ has to be considered:

$$h(\varphi) = \frac{4h_{\text{Spall}}}{\Delta\varphi^2}\left(\varphi^2 - \left(\Delta\varphi + 2\varphi_{def}\right)\varphi + \left(\varphi_{def}^2 + \Delta\varphi\varphi_{def}\right)\right) \tag{48}$$

One significant aspect, however, that has to be incorporated is the fact that due to the negligible size of real spalls compared to the dimension of the rolling element, only a fraction of the rolling element is able to follow the contour of the spall. In other words, only a small fraction of this element can enter the void. Therefore, for a given spall with the length s and a rolling element with the diameter D_{RE}, the maximum depth h (see Figures 10 and 11) can be computed as follows:

$$h = \frac{D_{RE}}{2} - \sqrt{\frac{D_{RE}^2}{4} - \frac{s^2}{4}} \tag{49}$$

3.4. Modelling of a fault on the inner ring of a bearing

The modelling of one or multiple faults on the inner ring of a bearing is achieved in a similar manner as previously shown with spalls on the outer ring. The only aspect that has to be taken into consideration is that the angular position of the spall φ_{def} is not at a fixed location, since the inner ring performs a rotational motion. In the vast majority of applications, the bearing's outer ring is fixed tightly inside an housing with zero rotational DOF. Hence, in this work, the reference frame is based on the stationary outer ring and not the inner one.

Therefore, the angular position of a fault on the inner ring is computed as follows:

$$\varphi_{def} = -\omega_s t, \tag{50}$$

where ω_s denotes the angular speed of the shaft (and therefore the inner ring) and the variable t denotes the elapsed time. The negative sign takes into account that a clockwise rotation of the shaft results in a counter-clockwise rotation of the rolling elements around their own axes.

In complete analogy to the previously depicted procedure about the simulation of triangular-shaped spalls (as illustrated in Figures 15 and 16) with the length s, the depth of the rolling element entering the void can be approximated in the following manner:

If $\varphi_{def} \leq \varphi \leq \left(\varphi_{def} + \frac{\Delta\varphi}{2}\right)$:

$$h(\varphi) = \left[\frac{D_{RE}}{2} - \sqrt{\frac{D_{RE}^2}{4} - \frac{s^2}{4}}\right] \frac{2}{\Delta\varphi}\left(\varphi - \varphi_{def}\right) \tag{51}$$

If $\left(\varphi_{def} + \frac{\Delta\varphi}{2}\right) \leq \varphi \leq \left(\varphi_{def} + \Delta\varphi\right)$:

$$h(\varphi) = \left[\frac{D_{RE}}{2} - \sqrt{\frac{D_{RE}^2}{4} - \frac{s^2}{4}}\right] \frac{2}{\Delta\varphi}\left(\varphi_{def} + \Delta\varphi - \varphi\right) \tag{52}$$

In addition to this, the height $h(\varphi)$ of a rolling element entering a parabolic-shaped spall is a function of φ and can be obtained via Eq. (48).

4. Numerical Results

A closer examination of Figures 12–14 unveils that the shape of the spall on the outer raceway has varying effects on the displacement of the outer ring in the y-direction. Therefore, a rectangular spall yields a more distinct influence

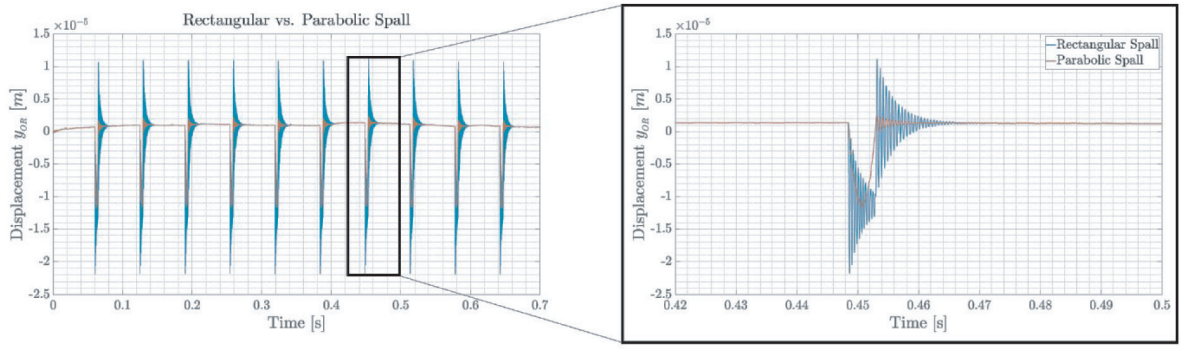

Figure 12. Comparison of the displacement of the outer ring (in y-direction) with rectangular- vs. parabolic-shaped spall on the outer raceway. Adapted from Floh and Weiss (2023).

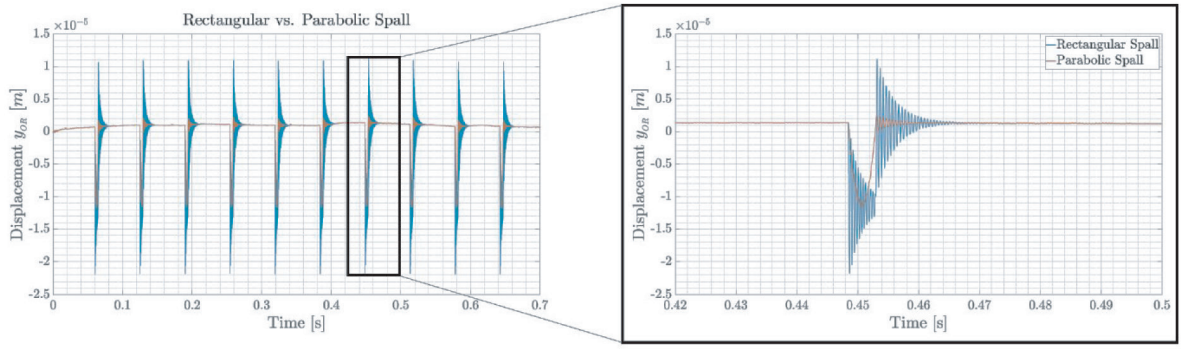

Figure 13. Comparison of the displacement of the outer ring (in y-direction) with rectangular- vs. triangular-shaped spall on the outer raceway. Adapted from Floh and Weiss (2023).

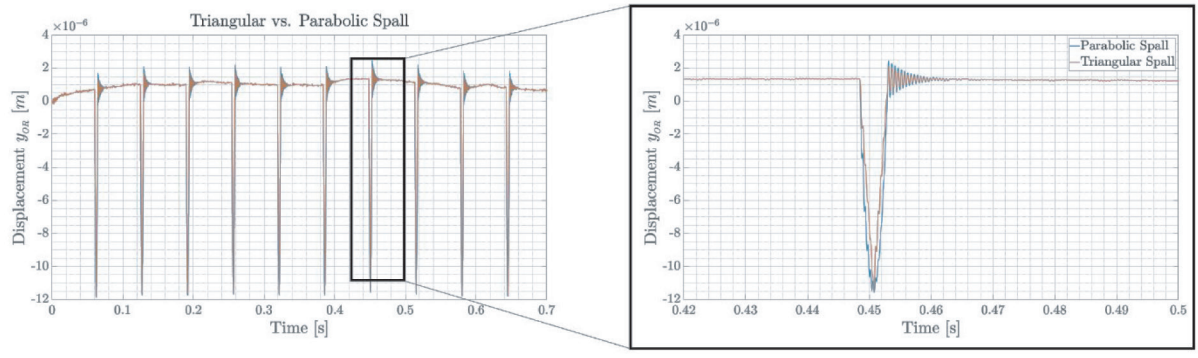

Figure 14. Comparison of the displacement of the outer ring (in y-direction) with triangular- vs. parabolic-shaped spall on the outer raceway. Adapted from Floh and Weiss (2023).

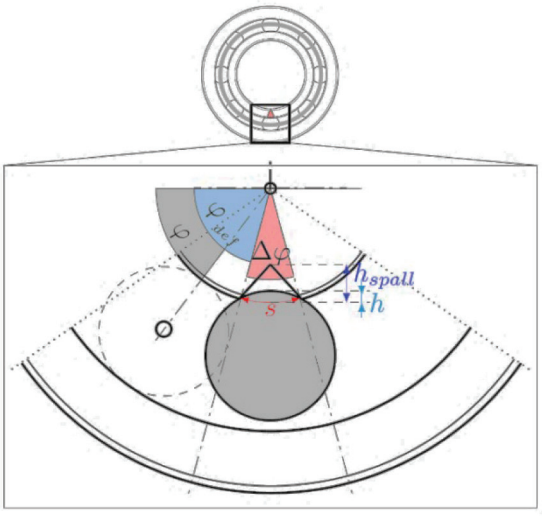

Figure 15. Illustration on how a rolling element approaches and enters a triangular spall in the inner ring. The dimensions of the spall are exaggerated for better demonstration.

compared to a parabolic- or triangular-shaped one, primarily due to the unrealistically sharp transitions, as illustrated in Figures 12 and 13. A subset of the simulation data is provided in Table 1.

Furthermore, Eq. (45) that incorporates the frictional torque T_{Fric} resulting from a spall in the outer raceway was calculated in Eq. (28). Therefore, this leads to a deviation in the rotational speed of the shaft, as

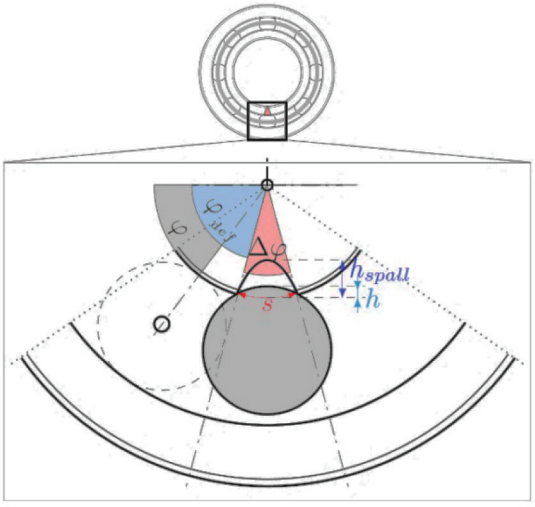

Figure 16. Illustration on how a rolling element approaches and enters a parabolic spall in the inner ring. The dimensions of the spall are exaggerated for better demonstration.

Table 1. Overview of the simulation data.

Quantity	Abbreviation	Value
Shaft speed	n_{Shaft}	300 rpm
Height spall	h_{Spall}	0.03715 mm
Width spall	s	1 mm
Diameter rolling element	D_{RE}	6.76 mm
Pitch diameter	D_{Pitch}	29.74 mm
Stiffness ball	k_{RE}	1.89×10^{10} N/m
Frictional coefficient	μ	0.001

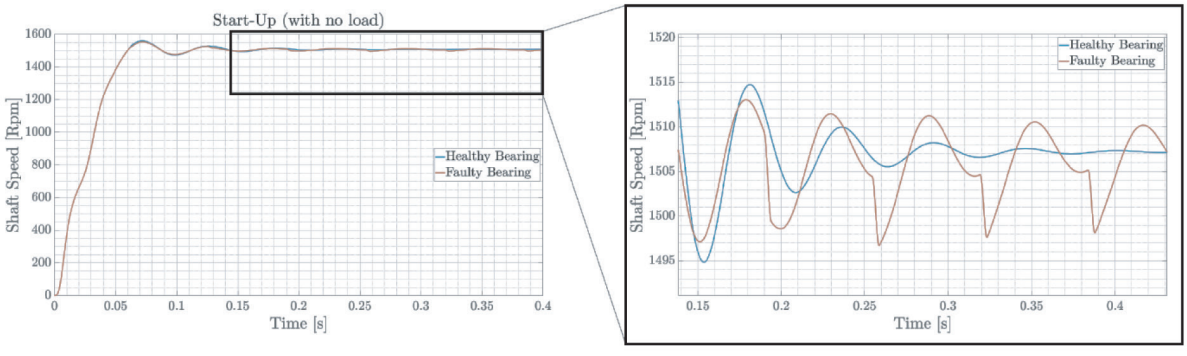

Figure 17. Visualisation of the shaft speed during the start-up of the motor without an attached load, comparing one with a healthy bearing to that with a faulty bearing (parabolic spall). Simulation parameters are given in Table 1. Adapted from Floh and Weiss (2023).

illustrated in Figure 17. In this investigation scenario, the average additional frictional torque is approximately 0.036 Nm.

An approach for the detection and characterisation of a fault in a bearing involves the analysis of the envelope spectrum of the acceleration signal (i.e. in the y-direction), as depicted in Figure 18. As shown in this plot, the presence of the first peak and its harmonics suggests a spall in the outer ring, which is backed by the evidence in this figure. In this illustration, the dominant peak aligns with the ball pass frequency of the outer

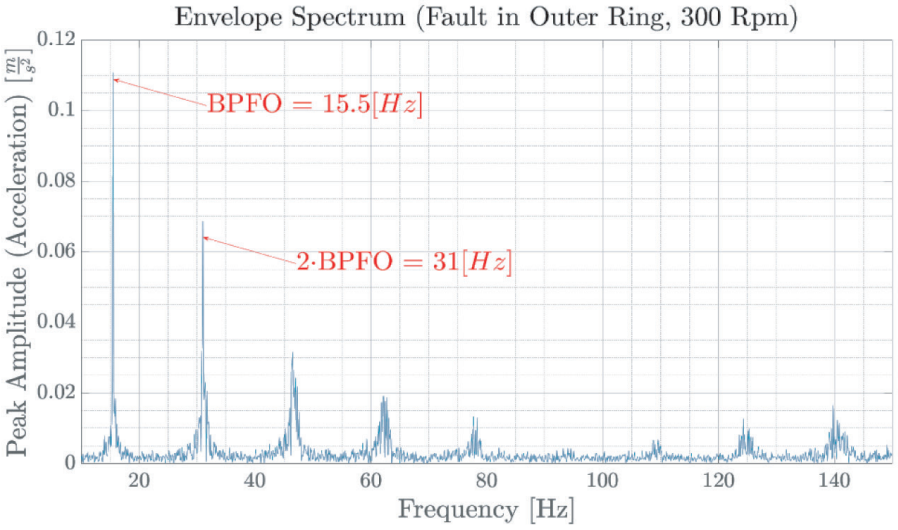

Figure 18. Envelope spectrum of the vibration signal (outer ring) in the y-direction of a bearing with a parabolic-shaped spall on the outer raceway and a shaft speed of 300 rpm. Adapted from Floh and Weiss (2023). BPFO, ball pass frequency of the outer ring.

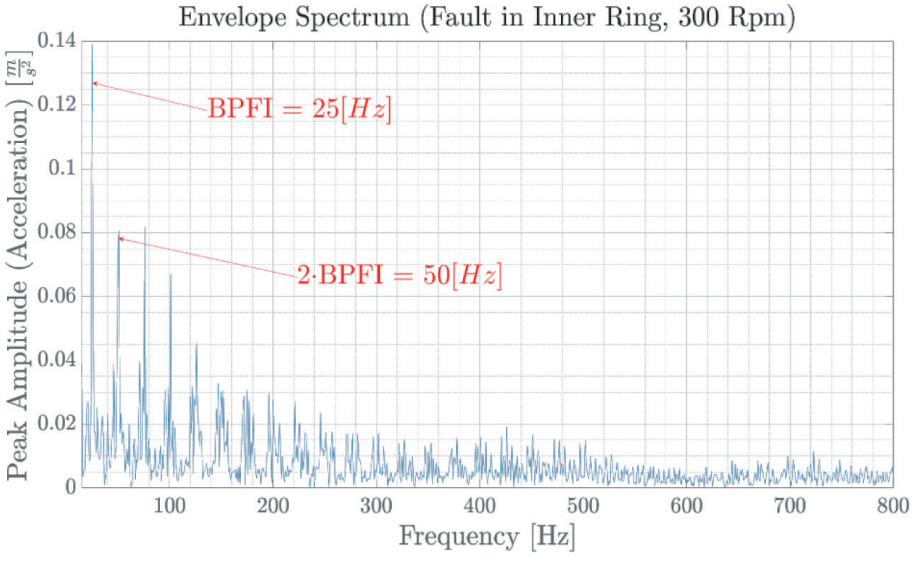

Figure 19. Envelope spectrum of the vibration signal (outer ring) in the y-direction of a bearing with a parabolic-shaped spall on the inner raceway and a shaft speed of 300 rpm. BPFI, ball pass frequency of the inner ring.

ring (BPFO), which can be obtained from the geometry of the bearing (see Table 1) and the following equation (Howard, 1994):

$$f_{\mathrm{BPFO}} = \frac{n_{RE}}{2} f_s \left(1 - \frac{D_{RE}}{D_{\mathrm{Pitch}}} \cos(\alpha)\right) \tag{53}$$

In complete analogy to Eq. (53), the ball pass frequency of the inner ring (BPFI) is given by the following relationship, which is beneficial for the characterisation of the fault shown in Figures 19 and 20 (Howard, 1994):

$$f_{\mathrm{BPFI}} = \frac{n_{RE}}{2} f_s \left(1 + \frac{D_{RE}}{D_{\mathrm{Pitch}}} \cos(\alpha)\right) \tag{54}$$

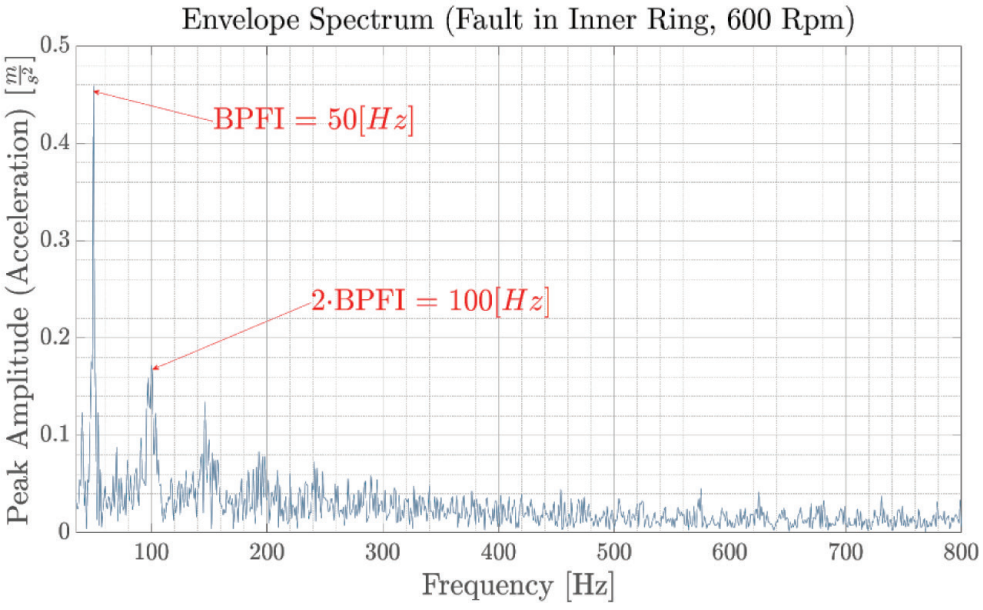

Figure 20. Envelope spectrum of the vibration signal (outer ring) in the y-direction of a bearing with a parabolic-shaped spall on the inner raceway and a shaft speed of 600 rpm. BPFI, ball pass frequency of the inner ring.

Figure 21. Bearing (6203-Z) with a rectangular spall (width s = 1.1 mm) perpendicular to the inner raceway. By utilising a polyamide cage, the bearing could be dismantled without damage.

5. Verification of the Bearing Model

The verification of the proposed bearing model in Section 3 has been accomplished with an experimental setup, mainly consisting of a bearing with a known fault, an housing, an electrical machine, an accelerometer and a corresponding measurement equipment. The purpose of the latter two is to keep track of the outer ring's vibration signal, which is then compared to the output of the simulation.

In the scope of this section, the following faults have been considered for the verification: a rectangular spall on the inner ring (Figure 21), and a parabolic spall each on the outer (Figure 22) and inner ring (Figure 23) of the bearing.

Even though the faults shown in Figures 21–23 are synthetically induced, they may resemble real faults, such as 'forced fracture', "false brinelling" or 'overload deformation' (plastic deformation), respectively (SKF, 2022).

Figure 22. Bearing (6203-Z) with a fault resembling a parabolic spall (width $s = 3.3$ mm) on the outer ring.

Figure 23. Bearing (6203-Z) with a fault resembling a parabolic spall (width $s = 3.4$ mm) on the inner ring.

The housing, which accommodates the examined bearings, is illustrated in Figure 24. In addition to this, an accelerometer The Kistler Group has its headquarters in Winterthur, Switzerland and is specialized on measurement technology (a KISTLER shear-type accelerometer) is mounted in close proximity to the bearing's outer ring.

The sensor signal is then recorded by a data acquisition module Hottinger Brüel and Kjaer Measurement Technology with its headquarters in Darmstadt, Germany (HBK QuantumX MX410B), which has a sampling rate of 200 kS/s and a vertical resolution of 24 bits.

Special care has to be taken that the angle of the defect that occurs (φ_{def}) in the experimental setting and the alignment of the rolling elements matches with that of the simulation. In addition to this, since the machine used in the verification process is an inverter-fed induction machine, the acceleration ramp and the exact rotational speed of the shaft also have to coincide with that of the simulation. Otherwise, an obvious shift between the measured and simulated data would be obtained.

To begin, the comparison of a bearing with a parabolic-shaped spall on the outer ring (see Figure 22) of the proposed simulation model and the experiment yields the results presented in Figure 25. Here, the majority of the peaks of the oscillations appear to be approximately in the same order of magnitude. Due to the random nature of the slippage (see Eq. [33]), a time shift between the oscillations occurs, which is visible at the beginning and the end of the recorded signal as shown in Figure 25.

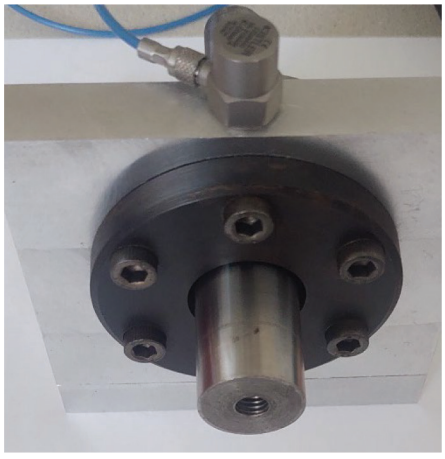

Figure 24. The housing of the examined bearings. The top centre of this illustration shows the mounted accelerometer.

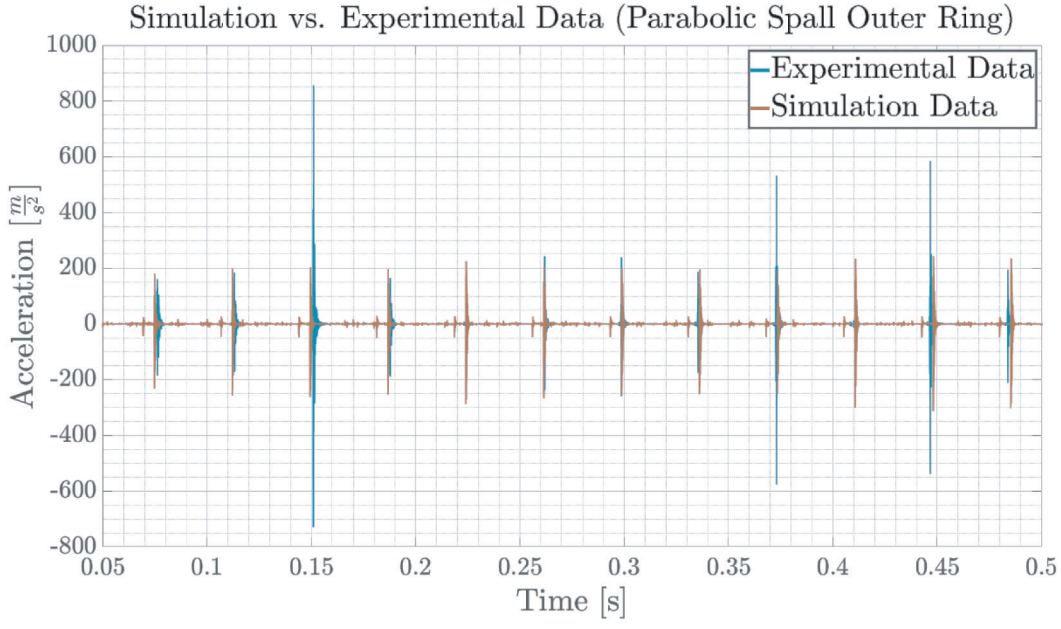

Figure 25. Comparison of the simulation and the experimental data of a parabolic spall on the outer raceway. Due to the rotational speed of the shaft (520 rpm), the inner ring performs approximately four revolutions in this recording.

The relatively high acceleration values in the experiments are caused due to the accelerometer mounted in close proximity to the outer ring and the shaft solely supported by the examined bearing, which therefore carries almost the entire weight of the shaft.

The next comparison aims to examine the difference between the simulation and the experiment of the parabolic-shaped spall on the inner ring (see Figure 23), as demonstrated in Figure 26.

Even though the majority of the oscillations' amplitudes are in the same order of magnitude, one significant difference occurs. Due to the fact that the massless rolling element in the simulation strictly follows the shape of the spall, an additional smaller oscillation occurs, whenever the rolling elements exit the spall. This described phenomenon is more pronounced, with such great spalls (and therefore great angular dimensions $\Delta\varphi$).

However, in real bearing applications, the rolling elements may not necessarily follow the shape of the entire spall. This assumption is backed by the data shown in Figure 26.

As initially stated in this work, the simulation of rectangular spalls yields unrealistic data, due to the occurrence of sharp transitions. Figure 27 supports this prediction, since the amplitudes of the simulation data are three to

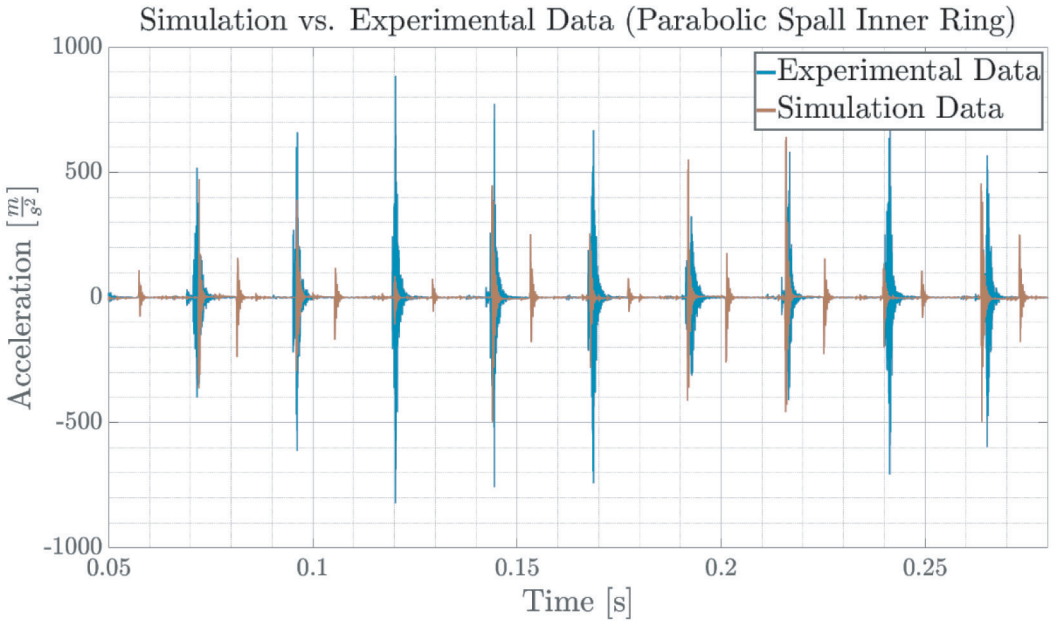

Figure 26. Comparison of the simulation and the experimental data of a parabolic spall on the inner raceway. Due to the rotational speed of the shaft (510 rpm), the inner ring performs approximately two revolutions in this recording.

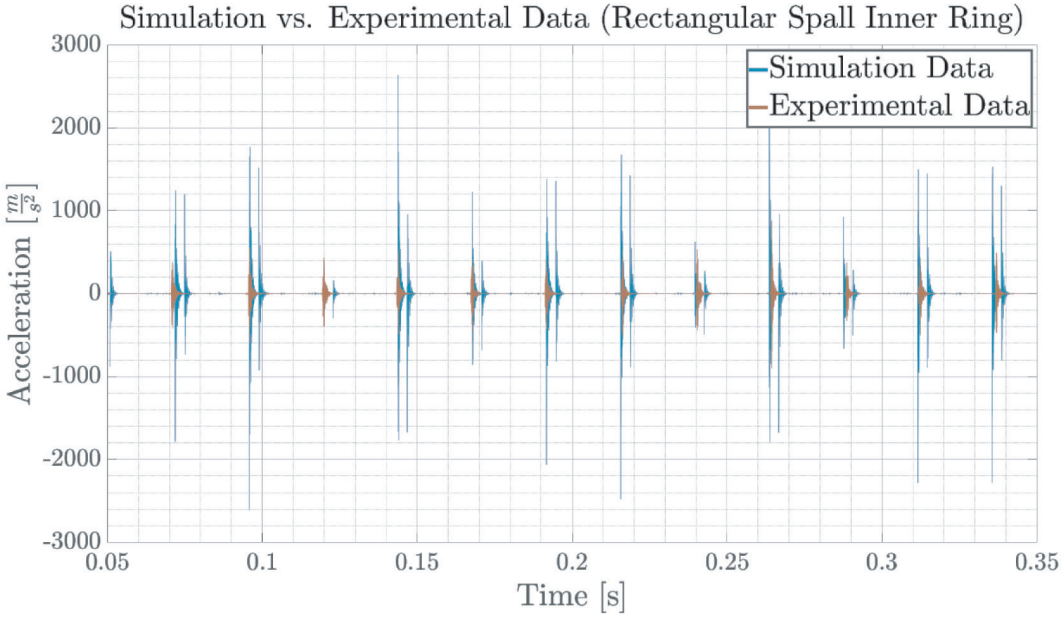

Figure 27. Comparison of the simulation and the experimental data of a rectangular spall on the inner raceway. Due to the rotational speed of the shaft (510 rpm), the inner ring performs approximately two revolutions in this recording.

four times greater than that of the experimental one, which is also true for the oscillations appearing as the rolling element exits the spall.

6. Conclusion

To foster the understanding of how different fault types affect the operation of induction machines, with respect to an additional frictional torque and vibration, the presented paper aims to introduce a method of simulating different

shapes of faults in a bearing raceway (both inner and outer ring) and examines their impact on the bearing as well as the machine as a whole.

Another benefit of a dynamic model lies in the possibility of obtaining synthetic vibration data, which can be utilised to evaluate and improve signal processing methods (both in the time and frequency domains) for detecting an (impending) fault in the examined bearing(s).

The first part of this work addresses the dynamic model of the induction machine featuring a squirrel cage rotor (with identified parameters from a 0.37 kW machine) that acts as a basis for the Simulink model. Subsequently, a bearing model with five DOF (five DOF of translational motion), along with the derived equations of motion as presented by Mishra et al. (2017) and Sawalhi and Randall (2008), is added to the Simulink model.

This work furthermore introduces and compares various shapes of faults in both inner and outer raceway. The findings demonstrate that sharp transitions associated with the rectangular spall result in significant oscillations of the (outer/inner) ring, leading to unrealistic results. In practical scenarios, however, the examined rolling element typically enters the spall gradually, rather than abruptly 'falling' into the void. Therefore, modelling a spall as triangular or parabolic (e.g. when simulating grooves) delivers more realistic outcomes. The additional frictional torque is then calculated as a consequence of the contact forces occurring between the rolling elements in the load zone and the raceway(s) in both the x- and y-directions. This torque is then utilised as an input of the induction machine model.

The final step covers the verification of the bearing model and the simulation of the proposed parabolic-shaped spalls in an experiment, which has been conducted with bearings of known fault size and shape. The outcome of the experiment shows that the simulation yields satisfying results with both spalls on the inner and outer ring.

In contrast, the limit of this simulation model clearly lies in the modelling of spalls with a sharp transition (such as rectangular-shaped ones) due to the occurrence of sharp transitions.

The future work on this topic could include an improvement of the machine model, covering non-linearities such as iron losses, current displacement or magnetic saturation. When it comes to the bearing model, one possible enhancement would be to consider gyroscopic motion of the rolling element in the presence of axial forces.

Fischer, R. (1995). *Elektrische Maschinen*. Wien München: Carl Hanser Verlag. [ISBN: 3-446-18423-18426]

References

Floh, F. and Weiss, H. (2023). On the simulation of bearing faults in induction machines. In: *Proceedings of the 36th International Conference on Electrical Drives and Power Electronics EDPE*. The High Tatras, 25–27 September 2023. doi: 10.1109/EDPE58625.2023.10274044.

Giersch, H. U., Harthus, H. and Vogelsang, N. (1991). *Elektrische Maschinen*. B.G. Teubner Stuttgart., Stuttgart. [ISBN: 3-519-26821-26823]

Gonzalo, A. (2017). Power Electronics and Electric Drives for Traction Application. Wiley, West Sussex. [ISBN: 978-1-118-95442-95443]

Gupta, P. K. (1975). Transient Ball Motion and Skid in Ball Bearings. *Journal of Lubrication Technology*, 97(2), pp. 261–269. doi: 10.1115/1.3452568

Gupta, P. K. (1979). Dynamics of Rolling Element Bearings Part I: Cylindrical Roller Bearing Analysis. *Journal of Lubrication Technology*, 101(3), pp. 293–302. doi: 10.1115/1.3453357

Howard, I. (1994). *A Review of Rolling Element Bearing Vibration 'Detection, Diagnosis and Prognosis'*. Australia: DSTO Aeronautical and Maritime Research Laboratory.

Krishnan, R. (2001). *Electric Motor Drives: Modeling, Analysis, and Control*. New Jersey: Prentice Hall. [ISBN: 978-0130910141]

Kumbhar, S. G., Sudhagar, E. and Desavale, R. G. (2021). An Overview of Dynamic Modeling of Rolling-Element Bearings. *Noise & Vibration Worldwide*, 52(1–2), pp. 3–18. doi: 10.1177/0957456520948279

Leedy, A. W. (2013). Simulink/ MATLAB Dynamic Induction Motor Model for Use as a Teaching and Research Tool. *International Journal of Soft Computing and Engineering (IJSCE)*, 3(4), pp. 102–108.

Lundberg, G. and Palmgren, A. (1947). Dynamic Capacity of Rolling Bearing. *Acta Polytechnic Mechanical Engineering Series*, 1(3), pp. 165-172

Meinel, A. (2020). Experimentelle Untersuchung der Auswirkungen von Axialschwingungen auf Reibung und Verschleiß in Zylinderrollenlagern. PhD-Thesis. Erlangen FAU University Press.

Mishra, C., Samantaray, A. K. and Chakraborty, G. (2017). Ball Bearing Defect Models: A Study of Simulated and Experimental Fault Signatures.

Journal of Sound and Vibration, 400, pp. 86–112. doi: 10.1016/j.jsv.2017.04.010

Nandi, S., Toliyat, H. A. and Li, X. (2005). Condition Monitoring and Fault Diagnosis of Electrical Motors – A Review. *IEEE Transactions on Energy Conversion*, 20(4), pp. 719–729. doi: 10.1109/TEC.2005.847955

Quang, N. P. and Dittrich, J. A. (2008). *Vector Control of Three-Phase AC Machines*. Springer, Heidelberg. [ISBN: 978-3-540-79028-79020]

Sawalhi, N. and Randall, R. B. (2008). Simulating Gear and Bearing Interactions in the Presence of Faults. Part I. The Combined Gear Bearing Dynamic Model and the Simulation of Localized Bearing Faults. *Mechanical Systems and Signal Processing*, 22(8), pp. 1924–1951. doi: 10.1016/j.ymssp.2007.12.001

SKF. (2022). Bearing Damage Analysis: ISO 15243 Is Here to Help You. *SKF Evolution*. Available at: https://evolution.skf.com/bearing-damage-analysis-iso-15243-is-here-to-help-you/. [Accessed 8 Sep. 2024].

Smagala, A. and Kecik, K. (2019). Nonlinear Model and Simulation of a Rolling Bearing. *IOP Conference Series Materials Science and Engineering*,710, pp. 1–8. doi: 10.1088/1757-899X/710/1/012006

Sopanen, J. and Mikkola, A. (2003a). Dynamic Model of a Deep Groove Ball Bearing Including Localized and Distributed Defects, Part 1: Theory. *Journal of Multi-body Dynamics*, 217(3), pp. 201–211. doi: 10.1243/14644190360713551

Sopanen, J. and Mikkola, A. (2003b). Dynamic Model of a Deep Groove Ball Bearing Including Localized and Distributed Defects, Part 2: Implementation and Results. *Journal of Multi-body Dynamics*, 217(3), pp. 213–223. doi: 10.1243/14644190360713560

Strangas, E. G., Clerc, G., Razik, H. and Soualhi, A. (2022). *Fault Diagnosis, Prognosis, and Reliability for Electrical Machines and Drives*. Wiley, Hoboken, New Jersey. [ISBN: 978-1-119-72275-72275]

Thorsen, V. and Dalva, M. (1995). A Survey of Faults on Induction Motors in Offshore Oil Industry, Petrochemical Industry, Gas Terminals, and Oil Refineries. *IEEE Transactions on Industry Applications*, 35(5), pp. 1186–1196. doi: 10.1109/28.464536